Computers and Fluids 124 (2016) 78–85

Contents lists available at ScienceDirect

Computers and Fluids

journal homepage: www.elsevier.com/locate/compfluid

Using quasi-DNS to investigate the deposition of elongated aerosol particles in a wavy channel flow

Gregory Lecrivain [a,b,*], Rohan Rayan [a], Antonio Hurtado [b], Uwe Hampel [a,c]

[a] Helmholtz-Zentrum Dresden-Rossendorf, Institut für Fluiddynamik, Bautzner Landstraße 400, Dresden 01328, Germany
[b] Technische Universität Dresden, Institut für Energietechnik, Professur für Wasserstoff- und Kernenergietechnik, Dresden 01062, Germany
[c] Technische Universität Dresden, Institut für Energietechnik, AREVA-Stiftungsprofessur für Bildgebende Messverfahren für die Energie- und Verfahrenstechnik, Dresden 01062, Germany

ARTICLE INFO

Article history:
Received 27 April 2015
Accepted 15 October 2015
Available online 10 November 2015

Keywords:
Graphite dust deposition
High temperature reactor
Quasi-DNS
Deposition of elongated particles
Wavy channel flow

ABSTRACT

In gas-cooled high temperature reactors, the diffusion of the fission products into the graphite matrix causes a radioactive contamination of the carbonaceous dust. The contaminated graphite aerosol particles often exhibit large aspect ratios and deposit in complex geometries, which hinders a detailed experimental investigation. The use of quasi Direct Numerical Simulation (quasi-DNS) to simulate the turbulent flow in nuclear reactors has seen an increased interest over the last few years. The capabilities of a quasi-DNS to simulate the transport and the deposition of elongated particles in a wavy channel flow are presently tested. It is shown that quasi-DNS effectively predicts deposition and that, unlike the deposition in a plane channel flow, the particle aspect ratio has no significant effect on the overall deposition rate in a wavy channel. It is suggested that in numerical studies of particle deposition on a significantly roughened channel, the particle can be assumed to be spherical without affecting the results of the deposition study.

1. Introduction

1.1. Motivations

Particle deposition denotes here the process of attaching suspended aerosol particles from a gas in turbulent motion to a wall surface. Once a particle comes into contact with the surface, attachment occurs due to surface forces such as van der Waals forces, capillary forces or electrostatic forces [1]. The transport and deposition of solid aerosol particles spans a wide range of industrial and non-industrial applications. It is used extensively in applications dealing with coal combustion [2], lung aerosol dynamics [3,4] and the sedimentation of atmospheric particles [5]. It also extends, as is the case here, to the deposition of aerosol graphite particles in the primary circuit of a High Temperature Reactor (HTR) [6]. The nuclear fuel particles are embedded in graphite, either as compacts to be placed in prismatic blocks or as pebbles [7]. Various experimental studies performed during reactor operations revealed the production and the deposition of carbonaceous dust in the primary circuit of the reactor. The carbonaceous dust very likely originated from the oxidation processes [8] and from the mechanical abrasion between the graphite components [9]. Findings from the work of Seeger et al. [10] showed that the fission products diffuse into the graphite matrix, resulting in a radioactive contamination of the carbonaceous dust. In a hypothetical severe accident such as a depressurisation in the HTR primary circuit, a sudden increase in the gas stream velocity may trigger the detachment of radioactive material of the particle deposit [11]. This re-entrained dose of contaminated dust may become a considerable source term upon escaping the system boundaries. Numerical modelling of these complex transport mechanisms are therefore of key importance to the HTR nuclear safety research assessment. Thus, it is critical to develop efficient and accurate numerical models capable of predicting the transport and the deposition of amorphous particles in turbulent flows.

1.2. Deposition of non-spherical particles

To date the deposition of graphite aerosol particles in the HTR circuits has largely been simulated by assuming that the particles where spherical in shape [12,13]. However, the experimental observations of Kugeler et al. [14] showed that graphite aerosol particles previously collected in the reactor circuit are usually randomly shaped and often exhibit high aspect ratios. The deposition of non-spherical particles has largely been simulated in plane channel flows [15] and in the lung systems [16]. The geometry of the gas-cooling system of a

* Corresponding author at: Helmholtz-Zentrum Dresden-Rossendorf, Institut für Fluiddynamik, Bautzner Landstraße 400, 01328 Dresden, Germany. Tel.: +49 351 260 3768; fax: +49 351 260 1 3768.
E-mail address: g.lecrivain@hzdr.de, gregory@cheme.kyoto-u.ac.jp (G. Lecrivain).

http://dx.doi.org/10.1016/j.compfluid.2015.10.012
0045-7930/

HTR, in which the contaminated particles are conveyed, can however often become complex. In a HTR, for which the fuel element is embedded in blocks, the heat transfer performance is often increased by artificially roughening the fuel rod surfaces [17,18]. In such systems the protrusions on the surfaces of fuel elements are used to disturb the viscous sublayer, which acts as an insulator because of the low thermal conductivity of the gas [19]. Very little is known on the deposition of particles with high aspect ratio in artificially roughened channel flows. The present work seeks to numerically assess the effect of the particle aspect ratio on the overall deposition rate in a wavy channel flow.

2. Methods

2.1. Continuous gas phase

Quasi Direct Numerical Simulation (quasi-DNS) has been increasingly used to simulate complex flows and heat transfers observed in various nuclear reactors [20]. The flow simulation in a limited HTR pebbled bed (i.e. a packing of spherical fuel elements) recently performed by Shams et al. [21,22] testifies to the increasing interest in the use of quasi-DNS. A conventional DNS with a spatial discretisation based on the finite volume method usually requires a very fine grid and a fourth-order interpolation scheme in the streamwise and spanwise wall directions [23,24], which in turn adversely affects the computational cost of the simulation. A quasi-DNS however implies an acceptable number of grid points, uses a second order central scheme with boundedness for spatial discretisation and a second order implicit scheme for temporal discretisation. It therefore offers a faster and accurate, yet not fully resolved flow simulation [25]. For an incompressible flow the governing equations are the continuity equation and the Navier–Stokes equation. The two equations read

$$\frac{\partial u_i}{\partial x_i} = 0, \tag{1}$$

$$\frac{\partial u_i}{\partial t} + \frac{\partial u_i u_j}{\partial x_j} = -\frac{1}{\rho}\frac{\partial p}{\partial x_i} + \nu\frac{\partial^2 u_i}{\partial x_j^2} + f_i. \tag{2}$$

The term u_i denotes the instantaneous fluid velocity in the x_i direction, t the time, ρ the fluid density, p the pressure and ν the kinematic viscosity. The forcing term $f_{i=1}$ represents the constant streamwise pressure gradient, enforced to drive the flow. The above equations were solved using the open source program OpenFOAM 2.1.1. For a detailed description of the finite-volume implementation and its discretisation schemes, the reader is referred to the thesis of de Villiers [26]. Not only has the above program seen an increasing deployment in the simulations of single-phase flows, it also has found recent application in the simulation of the low-inertia particle transport [27]. For these reasons, the present work nicely complements the study of Komen et al. [20], in which the performance of a quasi-DNS to study turbulent nuclear flows was tested. The present work therefore offers a new insight into the capabilities of the program to investigate the transport and, more importantly, the deposition of elongated particles in nuclear turbulent flows.

2.2. Spherical particles

In line with real experiments previously performed in HTR, the particle dilution is high [6]. This allows for a one-way coupling simulation, i.e. the influence of the particles on the continuous gas phase and the inter-particle interactions can be neglected. The molecular diffusion does not apply here since the particle size exceeds 1 μm [28]. The large particle-to-fluid density ratio S implies a negligible effect of the Saffman lift force on the overall particle deposition rate [29]. Thus retaining only the drag force $\boldsymbol{F}_D$ and the gravitational acceleration $\boldsymbol{g}$, the translational equation of motion of a particle evolving in the inertial xyz-coordinate system reads

$$\frac{\mathrm{d}\boldsymbol{v}}{\mathrm{d}t} = \boldsymbol{g} + \frac{\boldsymbol{F}_D}{m}, \tag{3}$$

where $\boldsymbol{v}$ is the particle velocity vector at the particle centroid and m the particle mass. For comparison purposes, the simulation is initially performed with spherical particles. The drag force $\boldsymbol{F}_D$ exerted on a spherical particle is given by

$$\boldsymbol{F}_D = \frac{1}{2}\rho\pi a^2 C_d |\boldsymbol{u} - \boldsymbol{v}|(\boldsymbol{u} - \boldsymbol{v}). \tag{4}$$

In the above formula the drag coefficient is derived from the semi-empirical formula of Schiller and Naumann

$$C_d = \frac{24}{Re_p}\left(1 + 0.15 Re_p^{0.687}\right). \tag{5}$$

The particle Reynolds number is defined as $Re_p = |\boldsymbol{u} - \boldsymbol{v}|2a/\nu$, where a is the particle radius.

2.3. Ellipsoidal particles

Experimental measurements performed during the corrosion process of graphite pebbles revealed large irregularities in the particle shape. The aspect ratio of graphite particles were found to often exceed the value of $\beta > 10$ [14]. A similar shape factor was also measured for graphite particles in the experimental test of Barth et al. [11]. In the present work, the needle-like elongated particles are modelled as prolate ellipsoids with semi-major axis b and semi-minor axis a. The aspect ratio of a particle is mathematically defined as $\beta = b/a$.

2.3.1. Coordinate systems

The governing equations of the gas phase (Eqs. (1) and (2)) together with the translation equations for particles are easily expressed in the *inertial coordinate system* $[x, y, z]$. The particle rotations are however expressed in a relatively simplistic fashion in the Lagrangian *particle coordinate system* $[\hat{x}, \hat{y}, \hat{z}]$. The particle coordinate system has its origin attached to the particle centre of mass and its $\hat{z}$-axis is aligned with the particle major axis. The *co-moving coordinate system* $[\hat{\hat{x}}, \hat{\hat{y}}, \hat{\hat{z}}]$ also moves with the particle. However, its three axes are parallel to those of the inertial coordinate system. The transformation between the particle coordinate system and the inertial coordinate system is expressed as

$$\hat{\boldsymbol{x}} = \boldsymbol{A} \cdot \boldsymbol{x}. \tag{6}$$

Bold letters are introduced to differentiate the matrices and the vectors from the scalar quantities. The three Euler angles (ψ, θ, ϕ) [30] are a natural candidate for the straightforward formulation of the transformation matrix $\boldsymbol{A} = \boldsymbol{A}(\psi, \theta, \phi)$. The use of the Euler angles have however proved unsuccessful in three-dimensional simulations because of the singularity problems that occurs whenever the azimuthal angle of the particles equals 0 or π [31]. The use of quaternions $\boldsymbol{q} = (q_1, q_2, q_3, q_0)$, whose four components satisfy $q_1^2 + q_2^2 + q_3^2 + q_0^2 = 1$, overcomes the singularity problem by rewriting the transformation matrix as follows

$$\boldsymbol{A} = \boldsymbol{A}(\boldsymbol{q}) = \begin{bmatrix} 1 - 2(q_2^2 + q_3^2) & 2(q_1 q_2 + q_3 q_0) & 2(q_1 q_3 - q_2 q_0) \\ 2(q_2 q_1 - q_3 q_0) & 1 - 2(q_3^2 + q_1^2) & 2(q_2 q_3 + q_1 q_0) \\ 2(q_3 q_1 + q_2 q_0) & 2(q_3 q_2 - q_1 q_0) & 1 - 2(q_1^2 + q_2^2) \end{bmatrix}. \tag{7}$$

Each component of the quaternion is defined as

$$\begin{aligned} q_1 &= \cos\frac{\phi - \psi}{2}\sin\frac{\theta}{2}, \quad q_2 = \sin\frac{\phi - \psi}{2}\sin\frac{\theta}{2} \\ q_3 &= \sin\frac{\phi + \psi}{2}\cos\frac{\theta}{2}, \quad q_0 = \cos\frac{\phi + \psi}{2}\cos\frac{\theta}{2}. \end{aligned} \tag{8}$$

2.3.2. Particle equations of motion

The rotational equations of motion of an ellipsoidal particle expressed in the particle $\hat{x}\hat{y}\hat{z}$-coordinate system are given as

$$I_{\hat{x}}\frac{\mathrm{d}\omega_{\hat{x}}}{\mathrm{d}t} - \omega_{\hat{y}}\omega_{\hat{z}}(I_{\hat{y}} - I_{\hat{z}}) = T_{\hat{x}}, \tag{9a}$$

$$I_{\hat{y}}\frac{\mathrm{d}\omega_{\hat{y}}}{\mathrm{d}t} - \omega_{\hat{z}}\omega_{\hat{x}}(I_{\hat{z}} - I_{\hat{x}}) = T_{\hat{y}}, \tag{9b}$$

$$I_{\hat{z}}\frac{\mathrm{d}\omega_{\hat{z}}}{\mathrm{d}t} - \omega_{\hat{x}}\omega_{\hat{y}}(I_{\hat{x}} - I_{\hat{y}}) = T_{\hat{z}}. \tag{9c}$$

The terms $I_{\hat{x}} = I_{\hat{y}} = ma^2(1+\beta^2)/5$ and $I_{\hat{z}} = 2ma^2/5$ are respectively the particle moments of inertia about the principal axes $\hat{x}$, $\hat{y}$ and $\hat{z}$. The terms $\boldsymbol{\omega} = (\omega_{\hat{x}}, \omega_{\hat{y}}, \omega_{\hat{z}})$ and $\boldsymbol{T} = (T_{\hat{x}}, T_{\hat{y}}, T_{\hat{z}})$ are respectively the particle angular velocities and the hydrodynamic torques acting on the particle with respect to the principal axes $\hat{x}$, $\hat{y}$ and $\hat{z}$. The time derivative of the quaternion $\dot{\boldsymbol{q}}$ can be expressed as a function of the particle angular velocity $\boldsymbol{\omega}$ as follows [32]

$$\dot{\boldsymbol{q}} = \begin{pmatrix} \dot{q}_1 \\ \dot{q}_2 \\ \dot{q}_3 \\ \dot{q}_0 \end{pmatrix} = \frac{1}{2}\begin{pmatrix} q_0\omega_{\hat{x}} - q_3\omega_{\hat{y}} + q_2\omega_{\hat{z}} \\ q_3\omega_{\hat{x}} + q_0\omega_{\hat{y}} - q_1\omega_{\hat{z}} \\ -q_2\omega_{\hat{x}} + q_1\omega_{\hat{y}} + q_0\omega_{\hat{z}} \\ -q_1\omega_{\hat{x}} - q_2\omega_{\hat{y}} - q_3\omega_{\hat{z}} \end{pmatrix}. \tag{10}$$

2.3.3. Force formulation

For an ellipsoidal particle moving in a Stokes flow, the drag force reads [33]

$$\boldsymbol{F}_D = \mu\ \pi\ a\ \boldsymbol{K}\cdot(\boldsymbol{u} - \boldsymbol{v}). \tag{11}$$

The term $\boldsymbol{K}$ is the resistance tensor, which in the inertial xyz-coordinate system is expressed as $\boldsymbol{K} = \boldsymbol{A}^{-1}\cdot\hat{\boldsymbol{K}}\cdot\boldsymbol{A}$. The components of the resistance diagonal tensor $\hat{\boldsymbol{K}}$ in the particle $\hat{x}\hat{y}\hat{z}$-coordinate system are given by

$$k_{\hat{x}\hat{x}} = k_{\hat{y}\hat{y}} = \frac{16(\beta^2-1)}{\left[(2\beta^2-3)\ln\left(\beta+\sqrt{\beta^2-1}\right)/\sqrt{\beta^2-1}\right]+\beta} \tag{12a}$$

$$k_{\hat{z}\hat{z}} = \frac{8(\beta^2-1)}{\left[(2\beta^2-1)\ln\left(\beta+\sqrt{\beta^2-1}\right)/\sqrt{\beta^2-1}\right]-\beta} \tag{12b}$$

2.3.4. Torque formulation

Assuming a linear shear flow in the direct vicinity of the particle, the three components of the torque $\boldsymbol{T}$ [34] are expressed in the particle $\hat{x}\hat{y}\hat{z}$-coordinate system as

$$T_{\hat{x}} = \frac{16\pi\mu a^3\beta}{3(\beta_0+\beta^2\gamma_0)}\left[(1-\beta^2)d_{\hat{z}\hat{y}} + (1+\beta^2)(w_{\hat{z}\hat{y}} - \omega_{\hat{x}})\right], \tag{13a}$$

$$T_{\hat{y}} = \frac{16\pi\mu a^3\beta}{3(\alpha_0+\beta^2\gamma_0)}\left[(\beta^2-1)d_{\hat{x}\hat{z}} + (1+\beta^2)(w_{\hat{x}\hat{z}} - \omega_{\hat{y}})\right], \tag{13b}$$

$$T_{\hat{z}} = \frac{32\pi\mu a^3\beta}{3(\alpha_0\beta_0)}(w_{\hat{y}\hat{x}} - \omega_{\hat{z}}). \tag{13c}$$

The terms $d_{\hat{i}\hat{j}} = 1/2(\partial u_{\hat{i}}/\partial x_{\hat{j}} + \partial u_{\hat{j}}/\partial x_{\hat{i}})$ and $w_{\hat{i}\hat{j}} = 1/2(\partial u_{\hat{i}}/\partial x_{\hat{j}} - \partial u_{\hat{j}}/\partial x_{\hat{i}})$ are the deformation tensor and the spin tensor respectively. The transformation of the flow velocity gradient $\boldsymbol{G}$ from the inertial xyz-coordinate system to the particle $\hat{x}\hat{y}\hat{z}$-coordinate system is calculated as follows $\boldsymbol{G}_{\hat{x}\hat{y}\hat{z}} = \boldsymbol{A}\cdot\boldsymbol{G}_{xyz}\cdot\boldsymbol{A}^{-1}$. The constants α_0, β_0 and γ_0 are given as

$$\alpha_0 = \beta_0 = \frac{\beta^2}{\beta^2-1} + \frac{\beta}{2(\beta^2-1)^{\frac{3}{2}}}ln\left[\frac{\beta-\sqrt{\beta^2-1}}{\beta+\sqrt{\beta^2-1}}\right] \tag{14a}$$

$$\gamma_0 = -\frac{2}{\beta^2-1} - \frac{\beta}{(\beta^2-1)^{\frac{3}{2}}}ln\left[\frac{\beta-\sqrt{\beta^2-1}}{\beta+\sqrt{\beta^2-1}}\right] \tag{14b}$$

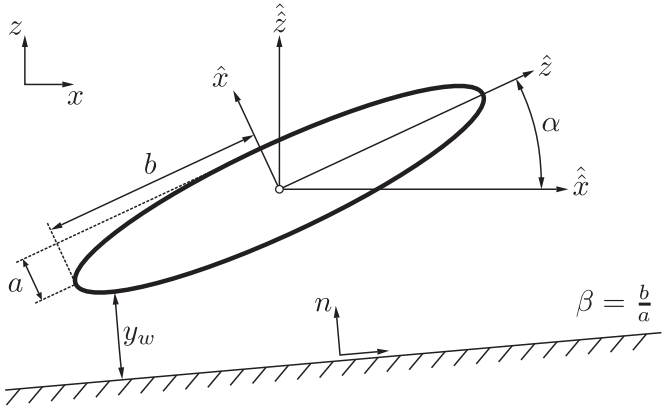

Fig. 1. Schematic diagram of an ellipsoidal particle near the wall.

2.3.5. Deposition criterion

The deposition criteria of a spherical particle colliding with the wall are fairly simple. A spherical particle will attach whenever the distance from the particle centre to the closest wall is lower than the particle radius [35]. The formulation becomes however complex when dealing with a prolate ellipsoid. In the present simulation, the mathematical formulation of the shortest distance from the particle boundary to the nearest wall is taken from the work of Fan and Ahmadi [36]. As seen in Fig. 1 the wall distance is a function of the two semi-axes of the prolate, the unit wall normal vector $\boldsymbol{n}$ and the inclination of the particle α relative the co-moving coordinate system. The distance y to the nearest wall is given by

$$y = \frac{-\xi(1/a^2-1/b^2)\sin\alpha\cos\alpha - \sqrt{(\cos\alpha/a)^2+(\sin\alpha/b)^2-[\xi/(ab)]^2}}{(\cos\alpha/a)^2+(\sin\alpha/b)^2}, \tag{15}$$

where the variable ξ is defined as

$$\xi = \sqrt{\frac{(b^2-a^2)^2\left[(\cos\alpha/a)^2+(\sin\alpha/b)^2\right]\cos^2\alpha\sin^2\alpha}{1+a^2b^2(1/a^2-1/b^2)^2\cos^2\alpha\sin^2\alpha}}. \tag{16}$$

The orientation α of the particle major axis is calculated as follows $\alpha = |\pi/2 - \cos^{-1}([\boldsymbol{A}^{-1}\cdot\hat{\boldsymbol{z}}]\cdot\boldsymbol{n})|$.

2.3.6. Numerical schemes

The present formulations used for the calculation of the hydrodynamic drag force and of the torque acting on a prolate ellipsoid were already introduced in previous simulations [15,37]. An implicit backward method is used for the computation of the particle velocity (Eq. 3) and of the particle rotation (Eqs. (9a)–(9c)). A fourth-order Runge–Kutta scheme is employed for the numerical integration of the quaternion (Eq. 10). A second-order Adams–Bashforth scheme is applied to compute the particle displacement.

2.3.7. Model validation

In the present section the in-house implementation of the particle transport model in OpenFOAM is tested against the numerical experiment of Chen and Yu [38]. In a horizontal circular duct, the motion of a single elongated particle was simulated. With a fluid kinematic viscosity $\nu = 10^{-5}\,\mathrm{m^2 s^{-1}}$ and a pipe radius of $R = 10^{-3}\,\mathrm{m}$, the bulk Reynolds number equalled $Re_b = 12$. x_1 corresponded to the streamwise direction of the laminar flow and x_2 to the gravity direction. A single particle with semi minor axis $b = 5\ \mu\mathrm{m}$, an aspect ratio of $\beta = 20$, a particle-to-fluid density ratio $S = 1000$ and an initial orientation $(\psi_0, \theta_0, \phi_0) = (45^\circ, -45^\circ, 0^\circ)$ was initially released in the flow at the position $x_3/R = 0.75$. The location and the orientation of the particle major axis as a function of time is illustrated in Fig. 2. The

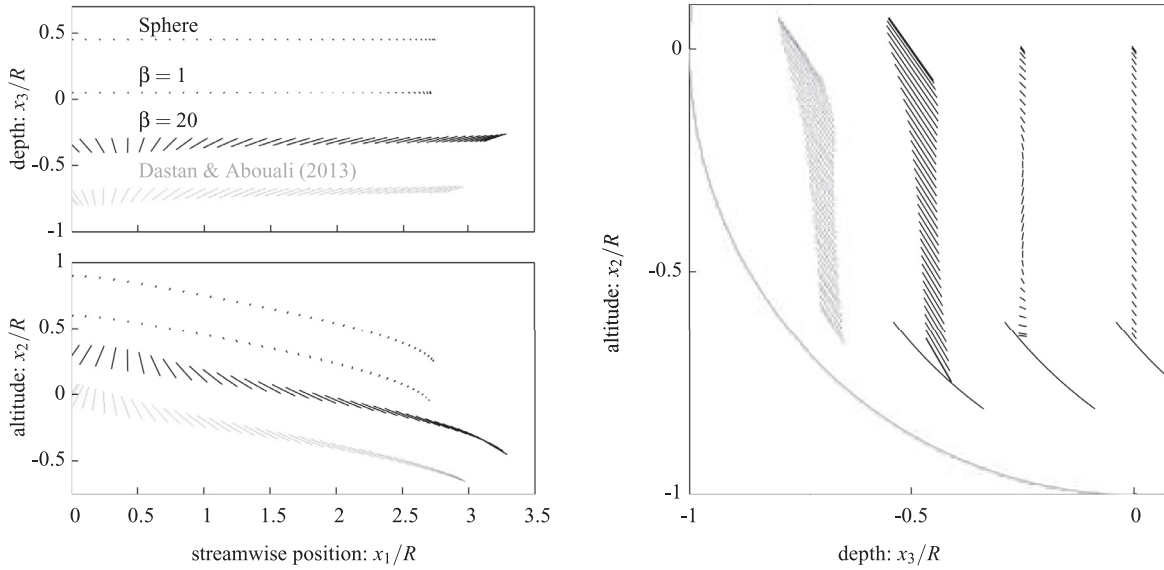

Fig. 2. Location and orientation of the major axis of an ellipsoidal particle. All particles are released at the location $(x_1, x_2, x_3) = (0, 0, -0.75R)$, where R is the pipe radius. The reference data [39] are coloured in grey. For comparison purposes the present simulated trajectories are shifted and shown in black.

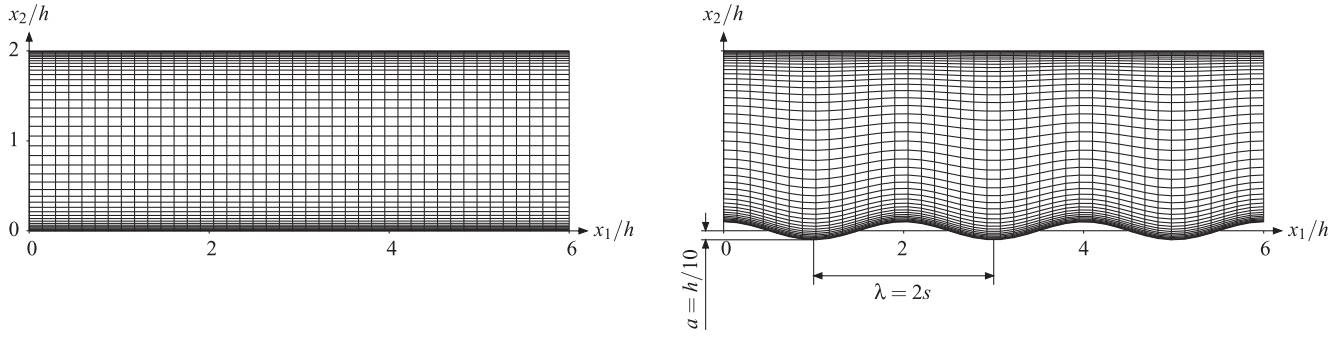

Fig. 3. Computational domain of the plane channel and of the wavy channel. For illustration purposes one third of the nodes are presently shown.

trajectory together with the orientation showed a very good agreement with the available literature data [39]. For comparison purposes the trajectories of a sphere and with the ellipsoidal model with $\beta = 1 - \epsilon$, where ϵ is an arbitrarily very small value. The response time for the sphere equalled that of the ellipsoid.

3. Results and discussions

The deposition of a cloud of elongated particles is investigated in a plane channel flow and in wavy channel of similar size. The deposition in the channel flow is initially used as validation. The effect of particle elongation is then investigated in the wavy channel flow. Fig. 3 shows a schematic of the two computational domains.

3.1. Plane channel flow

3.1.1. Geometry

The computational domain of the vertical plane channel flow consists of two parallel wall surfaces, separated by a distance $2h$. The length ratio and width ratio of the channel are set to $L_1/h = 6$ and to $L_3/h = 2.4$, respectively. For comparison [40] employed a spectral method to simulate the turbulent flow in channel, which had a height ratio equalled to $L_1/h = 6.4$ and width ratio equalled to $L_3/h = 3.2$. A periodic boundary condition is enforced in the streamwise and in the spanwise flow direction. The flow is simulated at Reynolds number $Re^* = 180$, based on the channel half-height h and the friction velocity u^*. The flow is driven by a constant pressure gradient $f_1 = u^{*2}/h$ (Eq. 2). The grid is stretched in the wall normal direction according a hyperbolic-tangent function with a stretching parameter of $\gamma = 2.8$ [41]. The node resolution of the grid is 128^3. The present grid node density in the streamwise direction is close to that used in the channel flow simulation of [24], who employed the finite difference method at the same Reynolds number $Re^* = 180$, with fourth-order accurate interpolations in the x_1- and x_3-directions and with a fourth-order spatial discretisation in the homogeneous directions.

3.1.2. Mean flow field and turbulence statistics

The time average streamwise fluid velocity $\overline{u}_1$ as a function of the normalised wall distance y^+ together with the turbulence intensities u_i' in the three space directions are shown in Fig. 4. The present results compare well with those taken from the available DNS database of Vreman and Kuerten [24]. The wall-normal RMS component u_2', which is of chief importance in the deposition process, matches remarkably well the reference points, and so does the spanwise component u_3'. It can be seen that the streamwise RMS component u_1' of the present quasi-DNS slightly underestimates the reference data. Gullbrand [41] also reported an underestimation of the streamwise velocity fluctuation in his quasi-DNS based on the finite difference method. It should be noted that the slight underestimation of the RMS velocity in the streamwise direction will not affect the deposition rate as long as the wall-normal RMS component is accurately predicted in the viscous sublayer [42].

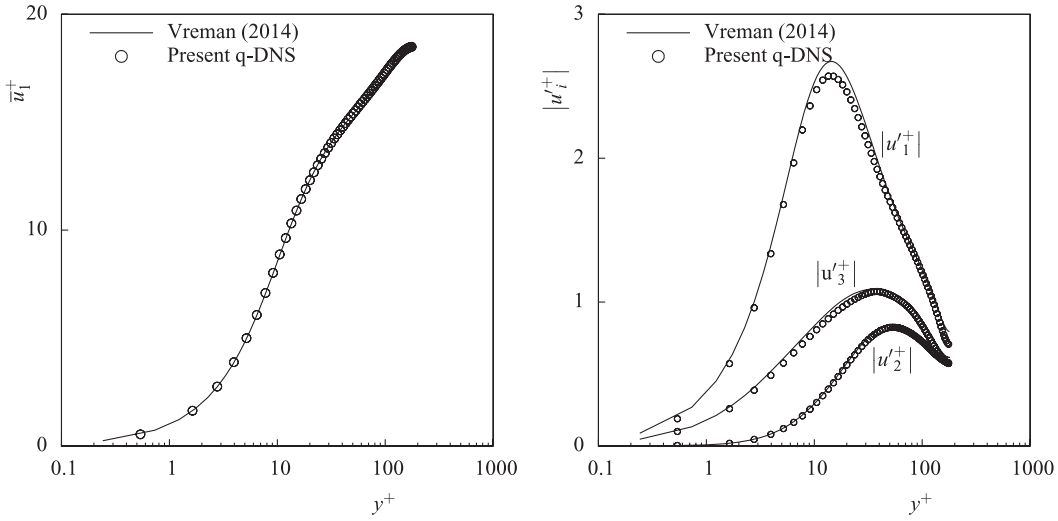

Fig. 4. Mean flow and RMS velocities in the plane channel flow.

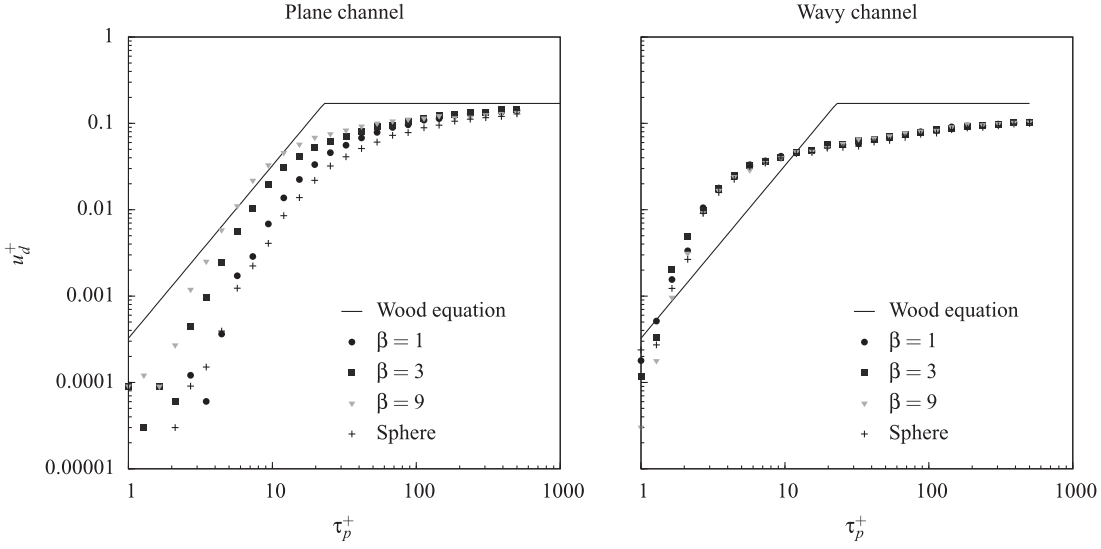

Fig. 5. Effect of the particle aspect ratio on the deposition velocity.

3.1.3. Particle deposition

The results of a deposition experiment are frequently plotted as curves of deposition velocity u_d against particle response time τ_p. The deposition velocity u_d is defined by the surface particle mass flux divided by the airborne particle mass concentration. As illustrated in Fig. 5, two deposition regimes typically exist in the present particle size range: the diffusion-impaction regime ($0.1 < \tau^+ < 10$) and the inertia-moderated regime ($10 < \tau^+ < 1000$) [43]. In the first diffusion-impaction regime the deposition velocity increases with increasing response time. As a result of the larger particle inertia in the second inertia-moderated regime the particle trajectories are less affected by near wall turbulence. The deposition velocity therefore is maximal and reaches an almost constant plateau. The equivalent response time [44] of an elongated particle is given by

$$\tau = \frac{S(2a)^2}{18\nu} \cdot \left(\beta \frac{\ln[\beta + \sqrt{\beta^2 - 1}]}{\sqrt{\beta^2 - 1}} \right). \tag{17}$$

When the particle aspect ratio β approaches unity the above Eq. (17) reduces to $\tau_p = S(2a)^2/(18\nu)$, which corresponds to the response time of a spherical particle of radius a. A cloud of N_0 particles, homogeneously distributed in space, was initially introduced into the channel domain. The initial particle velocity equalled that of the fluid and the particle orientation was randomly chosen. The simulation then ran for a time t, over which N_d particles deposited. The simulation time needed for the deposition corresponded to about $t = 1.4$ flow-through times. Over this time period it was ensured that the instantaneous number of particles $N(t)$ increased linearly with time. The deposition velocity [29] was then estimated as follows

$$u_d = -\frac{h}{2t} \ln\left(1 - \frac{N_d}{N_0}\right) \tag{18}$$

Fig. 5 shows the result of the deposition study carried out on particles of varying response times and aspect ratios which were released homogeneously in the plane channel. The empirical equation of Wood [45] is also shown for comparison purposes. While other experimental data are not shown here, it should be noted that estimations of the deposition velocity in a vertical turbulent flows exhibit a large scattering, which can cover as much as one to two orders of magnitudes [46]. In general, it is observed that the particle deposition velocity increases with increasing particle aspect ratio. It is also clearly observed that with increasing particle response time, the particle deposition velocity smoothly transitions from the diffusion impaction to the inertia moderated regime. It is also noteworthy that the effect of

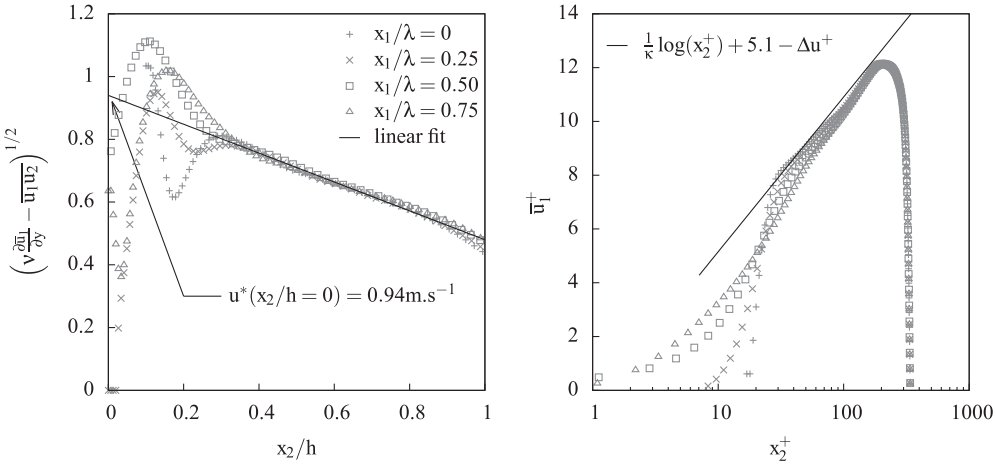

Fig. 6. Determination of the effective friction velocity $u^*(x_2/h = 0)$. The effective value $u^* = 1$ m s^{-1} exactly leads to the Reynolds number $Re^* = 180$. The right figure compares the mean streamwise flow velocity $\overline{u}_1$ with the empirical correlation derived in the transitionally rough regime [50]. The vertical shift in the streamwise velocity is given by $\Delta u^+ = \kappa^{-1} \log(1 + 0.26 k_s^+)$.

particle aspect ratio on deposition tends to diminish at higher values of particle response times. This suggests that the shape of larger particles (with response times well within the inertia moderated regime) does not influence the deposition characteristics in a plane channel.

3.2. Wavy channel flow

3.2.1. Geometry

The length, the width and the mean height of the wavy channel equal those of the plane channel. The upper channel surface is a flat wall and the altitude of the bottom wave takes the following cosine form

$$y_w(x_w) = a \cos\left(2\pi \frac{x_w}{\lambda}\right) \tag{19}$$

with $a/h = 0.1$ and $\lambda/h = 2$. Fig. 3 illustrates the geometry of the wavy channel. The bottom surface of the channel corresponds to that used in the experiment of Hudson et al. [47] and in the DNS of Cherukat et al. [48]. Both studies were performed under a higher Reynolds number $Re^* = 340$. For an open-channel with a wavy lower boundary the effective friction velocity is defined as

$$u^* = C\sqrt{h \frac{1}{\rho} \frac{dp}{dx_1}} = C\sqrt{h f_1}. \tag{20}$$

The constant C is a correction factor introduced by De Angelis et al. [49] to account for the effect of the ripples. With a ratio of $a/\lambda = 0.05$, De Angelis et al. [49] suggests $C = 0.81$. The forcing term f_1 in the streamwise direction could then be derived and placed in the momentum Eq. (2).

3.2.2. Mean flow field and turbulence statistics

The effective friction velocity u^* in a wavy channel flow is defined differently from that in a plane channel flow. Hudson et al. [47] introduced of a volume scalar field $u^*(\boldsymbol{x})$ which combines a Reynolds shear stress component and a viscous shear stress component. The field at a given point is given by

$$u^*(\boldsymbol{x}) = \sqrt{\nu \frac{\partial \overline{u}_1}{\partial x_1} - \overline{u_1 u_2}} \tag{21}$$

As one moves away from the wavy surface the time averaged streamwise velocity u_1 eventually exhibits a fairly linear variation with the wall vertical distance x_2. The approximately linear variation in the outer region can be used to define the friction velocity at the position $x_2/h = 0$ through the extrapolation of a liner fit

$$u^* = u^*(x_2/h = 0). \tag{22}$$

The present linear extrapolation shown in Fig. 6 delivers an effective friction velocity 6% lower than the expected value, resulting in a Reynolds number $Re^* = 173$. Fig. 6 also shows the mean streamwise fluid velocity as a function of the wall normal distance. It can be seen that the data compare well with the empirical correlation cited in the review of Jimenez [50] for transitionally rough wall

$$\overline{u}_1^+ = \frac{1}{\kappa} \log(x_2^+) + 5.1 - \Delta u^+. \tag{23}$$

In the above formula $\kappa = 0.4$ is the van Karman constant and $\Delta u^+ = \kappa^{-1} \log(1 + 0.26 k_s^+)$ is a vertical velocity shift. The term $k_s^+ = 2au^*/\nu = 36$ is here the equivalent roughness of the wavy surface. A direct comparison with the numerical data of Cherukat et al. [48], who performed a direct numerical simulation in the exact same channel flow at a higher Reynolds number $Re^* = 360$, is not appropriate because it was performed in a fully rough regime, i.e. for $k_s^+ > 70$.

3.2.3. Particle deposition

As in the case of deposition in the plane channel, the deposition velocities of particles with a wide range of particle response times are calculated again for the artificially roughened channel. As in the case of the plane channel, it is seen that deposition occurs in two regimes, namely, the diffusion-impaction and the inertia-moderated regime. Unlike the plane channel, it is observed that the deposition velocity is larger in the case of the wavy channel and particles transition into the inertia-moderated regime at a lower particle response time. This is consistent with the results obtained by Li and Ahmadi [51], for deposition of spherical particles in a less roughened channel. The increase in deposition is due to the fact that as the roughness increases, the turbulence intensity increases as well. This causes the turbulence dispersion to be more effective which in turn causes the diffusion impaction process to become more dominant, even for relatively smaller particles (particles with lower response times). Another cause of this effect can also be attributed to the increase in particle capture distance from the wall as the wall roughness increases. Thus, it is observed in Fig. 5 that the transition into the impaction regime occurs at τ_p^+ in range as low as $4 - 5$. In this study, it is observed that the particle deposition is unaffected by the particle aspect ratio has also seen in Fig. 5. Thus it is concluded that the determining factor in the deposition of particles in a wavy turbulent channel is the particle response time and not the particle shape. This result has practical implications

for further studies involving highly roughened channels where the shape of the particle can be neglected and the results still deliver reliable deposition data.

4. Conclusions

The objective of this work was to numerically investigate the effect of particle aspect ratio on the deposition in a wavy channel flow. The continuous gas phase was modelled using a quasi-DNS approach which allowed a lower computational cost. The flow characteristics using this approach was compared to the DNS database of Vreman Kuerten [24]. It was seen that the critical wall-normal component of velocity matched the reference data exceedingly well. The particles were modelled as prolate ellipsoids which were associated with translation and rotational motion. A quaternion based Lagrangian method was used to model the motion of the particle in the gas phase. This model was then validated using the numerical experiment of Chen and Yu [38]. It was seen that this data corresponds well with the available reference data. The deposition of ellipsoidal particles with various response times, was studied in a plane and wavy channels of similar sizes. In general, it is seen that the particle deposition in a plane channel increases with increase in particle aspect ratio but this effect diminishes with increasing particle response time. Whereas, in a highly roughened channel, the deposition velocity is unaffected by the particle aspect ratio. This data obtained under high roughness can be used as a model validation of Reynolds-averaged Navier–Stokes simulations, especially for near wall corrections. The results have direct application to high temperature reactor since, the particles are usually non spherical. Thus, it is suggested that in numerical studies of particle deposition on a significantly roughened channel, the particle can be assumed to be spherical without affecting the results of the deposition study. Such an assumption can also be safely made in a plane channel when it is determined that the size of the particles lies well within the inertia-moderated regime. This would lead to significant savings in computational costs as the equations concerning the rotation of the particles need not be computed. This work also tested the capability of OpenFOAM to compute the quasi-DNS equations gas phase as well as the Lagrangian equations for the ellipsoidal particles. It is seen that the performance of this solver is adequate and it corresponds well with the data produced in the literature for such simulations.

Acknowledgements

This work was supported by the European Commission under the grant no. 249337 of the Thermal Hydraulics of Innovative Nuclear Systems research project and by the Projektträger Reaktorsicherheitsforschung (PTR) des Bundesministeriums für Wirtschaft und Technologie (BMWi) under the grant no. 1501429.

References

[1] Kordecki MC, Orr C. Adhesion of solid particles to solid surfaces. Arch Environ Health Int J 1960;1:1–9.
[2] Lee FCC, Lockwood FC. Modelling ash deposition in pulverized coal-fired applications. Prog Energy Combust Sci 1998;25:117–32.
[3] Hofmann W. Modelling inhaled particle deposition in the human lung - A review. J Aerosol Sci 2011;42:693–724.
[4] Soni B, Aliabadi S. Large-scale CFD simulations of airflow and particle deposition in lung airway. Comput Fluids 2013;88:804–12.
[5] Noll KE, Fang KYP, Watkins LA. Characterization of the deposition of particles from the atmosphere to a flat plate. Atmos Environ 1988;22:1461–8.
[6] Moormann R. Fission product transport and source terms in HTRs: experience from AVR pebble bed reactor. Sci Technol Nucl Install 2008;2008:1–14.
[7] Tak N, Kim M, Lee WJ. Numerical investigation of a heat transfer within the prismatic fuel assembly of a very high temperature reactor. Ann Nucl Energy 2008;35:1892–9.
[8] Nieder R. Conclusions for high-temperature reactor chemistry drawn from 21 operating years of the AVR reactor. In: Proceedings of the VGB conference on power plant chemistry; 1990.
[9] Kissane MP. A review of radionuclide behaviour in the primary system of a very-high-temperature reactor. Nucl Eng Des 2009;239:3076–91.
[10] Seeger O, Knebel K, de Weerd W, Carbol P, Bottomley PDW, Rondinella VV, et al. Simulated accident testing of a fuel element from the HFR-EU1bis irradiation campaign. Nucl Eng Des 2014;271:171–9.
[11] Barth T, Kulenkampff J, Bras S, Gründig M, Lippmann-Pipke J, Hampel U. Positron emission tomography in pebble beds. Part 2. Graphite particle deposition and resuspension. Nucl Eng Des 2014;267:227–37.
[12] Lecrivain G, Drapeau-Martin S, Barth T, Hampel U. Numerical simulation of multilayer deposition in an obstructed channel flow. Adv Powder Technol 2014;25:310–20.
[13] Lecrivain G, Barry L, Hampel U. Three-dimensional simulation of multilayer particle deposition in an obstructed channel flow. Powder Technol 2014;258:134–43.
[14] Kugeler K, Epping C, Roes J. Importance of radioactive aerosols in hypothetical high temperature reactor accidents. J Aerosol Sci 1989;20:1421–4.
[15] Zhang H, Ahmadi G, Fan F, McLaughlin JB. Ellipsoidal particles transport and deposition in turbulent channel flows. Int J Multiph Flow 2001;27:971–1009.
[16] Feng Y, Kleinstreuer C. Analysis of non-spherical particle transport in complex internal shear flows. Phys Fluids 2013;25:1–26.091904
[17] Mingaleeva GS, Mironov YuV, Razina NS, Fomicheva TI. Heat transfer in gas-cooled assemblies with artificial roughness. Sov At Energy 1981;51:805–6.
[18] Takase K. Experimental and analytical studies on turbulent heat transfer performance of a fuel rod with spacer ribs for high temperature gas-cooled reactors. Nucl Eng Des 1995;154:345–56.
[19] Hassan MA, Rehme K. Heat transfer near spacer grids in gas-cooled rod bundles. Nucl Technol 1981;52:401–14.
[20] Komen E, Shams A, Camilo L, Koren B. Quasi-DNS capabilities of OpenFOAM for different mesh types. Comput Fluids 2014;96:87–104.
[21] Shams A, Roelofs F, Komen EMJ, Baglietto E. Quasi-direct numerical simulation of a pebble bed configuration. Part I. Flow (velocity) field analysis. Nucl Eng Des 2013;263:473–89.
[22] Shams A, Roelofs F, Komen EMJ, Baglietto E. Quasi-direct numerical simulation of a pebble bed configuration. Part II. Temperature field analysis. Nucl Eng Des 2013;263:490–9.
[23] Kozuka M, Seki Y, Kawamura H. DNS of turbulent heat transfer in a channel flow with a high spatial resolution. Int J Heat Fluid Flow 2009;30:514–24.
[24] Vreman AW, Kuerten JGM. Comparison of direct numerical simulation databases of turbulent channel flow at $Re_\tau = 180$. Phys Fluids 2014;26:1–21.015102
[25] Shams A, Roelofs F, Komen EMJ, Baglietto E. Optimization of a pebble bed configuration for quasi-direct numerical simulation. Nucl Eng Des 2012;242:331–40.
[26] de Villiers E. The potential of large eddy simulation for the modeling of wall bounded flows. Imperial College, London (UK); 2006. Dissertation.
[27] Flores F, Garreaud R, Muñoz RC. OpenFOAM applied to the CFD simulation of turbulent buoyant atmospheric flows and pollutant dispersion inside large open pit mines under intense insolation. Comput Fluids 2014;90:72–87.
[28] Ounis H, Ahmadi G, McLaughlin JB. Brownian diffusion of submicrometer particles in the viscous sublayer. J Colloid Interface Sci 1991;143:266–77.
[29] Uijttewaal WSJ, Oliemans RVA. Particle dispersion and deposition in direct numerical and large eddy simulations of vertical pipe flows. Phys Fluids 1996;8:2590–604.
[30] Goldstein H, Poole CP, Safko JK. Classical mechanics. Addison-Wesley; 1980.
[31] Njobuenwu DO, Fairweather M. Effect of shape on inertial particle dynamics in a channel flow. Flow Turbul Combust 2014;92:83–101.
[32] Kleinstreuer C, Feng Y. Computational analysis of non-spherical particle transport and deposition in shear flow with application to lung aerosol dynamics – a review. ASME J Biomech Eng 2013;135:1–19.
[33] Brenner H. The Stokes resistance of an arbitrary particle. IV. Arbitrary fields of flow. Chem Eng Sci 1964;19:703–27.
[34] Jeffery GB. The motion of ellipsoidal particles immersed in a viscous fluid. Proc R Soc Lond Ser A Contain Pap Math Phys Character 1922;102:161–79.
[35] Lecrivain G, Hampel U. Influence of the Lagrangian integral time scale estimation in the near wall region on particle deposition. ASME J Fluids Eng 2012;134:1–6.
[36] Fan F, Ahmadi G. A sublayer model for wall deposition of ellipsoidal particles in turbulent streams. J Aerosol Sci 1995;26:813–40.
[37] Marchioli C, Fantoni M, Soldati A. Orientation, distribution, and deposition of elongated, inertial fibers in turbulent channel flow. Phys Fluids 2010;22:1–14.033301
[38] Chen YK, Yu CP. Sedimentation of fibers from laminar flows in a horizontal circular duct. Aerosol Sci Technol 1991;14:343–7.
[39] Dastan A, Abouali O. Microfiber motion and web formation in a microchannel heat sink: a numerical approach. Comput Fluids 2013;71:28–40.
[40] Abe H, Kawamura H, Matsuo Y. Direct numerical simulation of a fully developed turbulent channel flow with respect to the Reynolds number dependence. ASME J Fluids Eng 2001;123:382–93.
[41] Gullbrand J. An evaluation of a conservative fourth order DNS code in turbulent channel flow. Annual research briefs. Center for Turbulence Research; 2000. p. 211–18.
[42] Tian L, Ahmadi G. Particle deposition in turbulent duct flows – comparisons of different model predictions. J Aerosol Sci 2007;38:377–97.
[43] Nerisson P, Simonin O, Ricciardi L, Douce A, Fazileabasse J. Improved CFD transport and boundary conditions models for low-inertia particles. Comput Fluids 2011;40:79–91.
[44] Shapiro MI, Goldenberg M. Deposition of glass fiber particles from turbulent air flow in a pipe. J Aerosol Sci 1993;24:65–87.
[45] Wood NB. A simple method for the calculation of turbulent deposition to smooth and rough surfaces. J Aerosol Sci 1981;12:275–90.

[46] Papavergos P, Hedley A. Particle deposition behaviour from turbulent flows. Chem Eng Res Des 1984;62:275–95.
[47] Hudson JD, Dykhno L, Hanratty TJ. Turbulence production in flow over a wavy wall. Exp Fluids 1996;20:257–65.
[48] Cherukat P, Na Y, Hanratty TJ, McLaughlin JB. Direct numerical simulation of a fully developed turbulent flow over a wavy wall. Theor Comput Fluid Dyn 1998;11:109–34.
[49] De Angelis V, Lombardi P, Banerjee S. Direct numerical simulation of turbulent flow over a wavy wall. Phys Fluids 1997;9:2429–42.
[50] Jimenez J. Turbulent flows over rough walls. Annu Rev Fluid Mech 2004;36:173–96.
[51] Li A, Ahmadi G. Computer simulation of deposition of aerosols in a turbulent channel flow with rough walls. Aerosol Sci Technol 1993;18:11–24.